ORIGINAL RESEARCH ARTICLE

Assessing the Effects of Chemical Composition and Short-Range Ordering on the Tensile Deformation Behavior of Nanocrystalline High-Entropy Alloys Nb–Ta–Hf–Zr: A Combined Study on Molecular Dynamics and Monte Carlo Simulation

RITA I. BABICHEVA, AJAY KUMAR, RAJ KIRAN, SERGEY V. DMITRIEV, ARTEM A. IZOSIMOV, and ELENA A. KORZNIKOVA

In the work, simulations using Monte Carlo (MC) and molecular dynamics (MD) methods are carried out to investigate the Nb–Ta–Hf–Zr system refractory high-entropy alloys (HEAs). In particular, the effects of chemical composition and grain boundary (GB) network on short-range ordering (SRO) during combined MC/MD modeling of relaxation mimicking diffusion process are investigated on single-crystalline and nanocrystalline (NC) HEAs. In addition, using MD modeling, the influence of SRO on the mechanical behavior of NC HEAs $(NbTa)_{50}$–Hf_{25}–Zr_{25}, $(NbTa)_{90}$–Hf_5–Zr_5, $(NbTa)_{50}$–Hf_{45}–Zr_5, and $(NbTa)_{50}$–Hf_5–Zr_{45} subjected to the high-temperature (1000 K) uniaxial tensile loading is studied in comparison with corresponding alloys without preliminary MC/MD relaxation. It is revealed that the level of SRO of certain elements is dictated by their content in a material; the lower the number of atoms forming ordered clusters, the higher the tendency to form such clusters. Along with some nano-conglomerates formed by solely Nb, Ta, Hf, and Zr atoms, the MC/MD relaxation results in SRO of Zr with Hf and Nb with Ta in coherent nanoclusters having the B2 lattice. The presence of a dense GB network can significantly affect the SRO process; Zr, Nb, and Hf segregate to GBs, but they are depleted of Ta atoms. Such distribution of atoms in NC samples is mainly dictated by the difference in atomic sizes and chemical affinity between constituent elements. Results of MD modeling of tensile deformation for the relaxed and non-relaxed NC HEAs show that SRO strengthens the alloys, increasing the yield strength, especially in equiatomic alloy and in $(NbTa)_{50}$–Hf_{45}–Zr_5. This is explained by both the formation of GB segregations and the enrichment of grains by Ta atoms, enhancing the body-centered cubic structure stability and, therefore, inhibiting preliminary phase transition and dislocation nucleation. Meanwhile, coherent B2 particles of NbTa can lead to additional strengthening of the HEAs through the load transfer mechanism. The work sheds light on the high-temperature mechanical behavior of Nb–Ti–Hf–Zr-based HEAs and can be used as a guide in the development of advanced HEAs for high-performance applications.

RITA I. BABICHEVA is with the Laboratory for Metals and Alloys under Extreme Impacts, Ufa University of Science and Technology, Ufa, 450076 Russia and also with the Institute of Molecule and Crystal Physics, Ufa Federal Research Center of Russian Academy of Sciences, Ufa, 450075 Russia. AJAY KUMAR and RAJ KIRAN are with the School of Mechanical and Materials Engineering, Indian Institute of Technology Mandi, Mandi, Himachal Pradesh 175005, India. Contact e-mail: raj@iitmandi.ac.in SERGEY V. DMITRIEV is with the Institute of Molecule and Crystal Physics, Ufa Federal Research Center of Russian Academy of Sciences and also with the Ufa State Petroleum Technological University, Ufa, 450062 Russia. ARTEM A. IZOSIMOV is with the Bashkir State Medical University, Ufa, 450008 Russian Federation. ELENA A. KORZNIKOVA is with the Laboratory for Metals and Alloys under Extreme Impacts, Ufa University of Science and Technology and also with the National Research University Higher School of Economics, St-Petersburg, St. Petersburg, 194100 Russia and also with the Politechnical Institute (branch) of M.K. Ammosov North-Eastern Federal University, Mirny, 678179 Russia. Contact e-mail: elena.a.korznikova@gmail.com

Manuscript submitted June 19, 2025; accepted September 28, 2025.

Published online: 13 October 2025

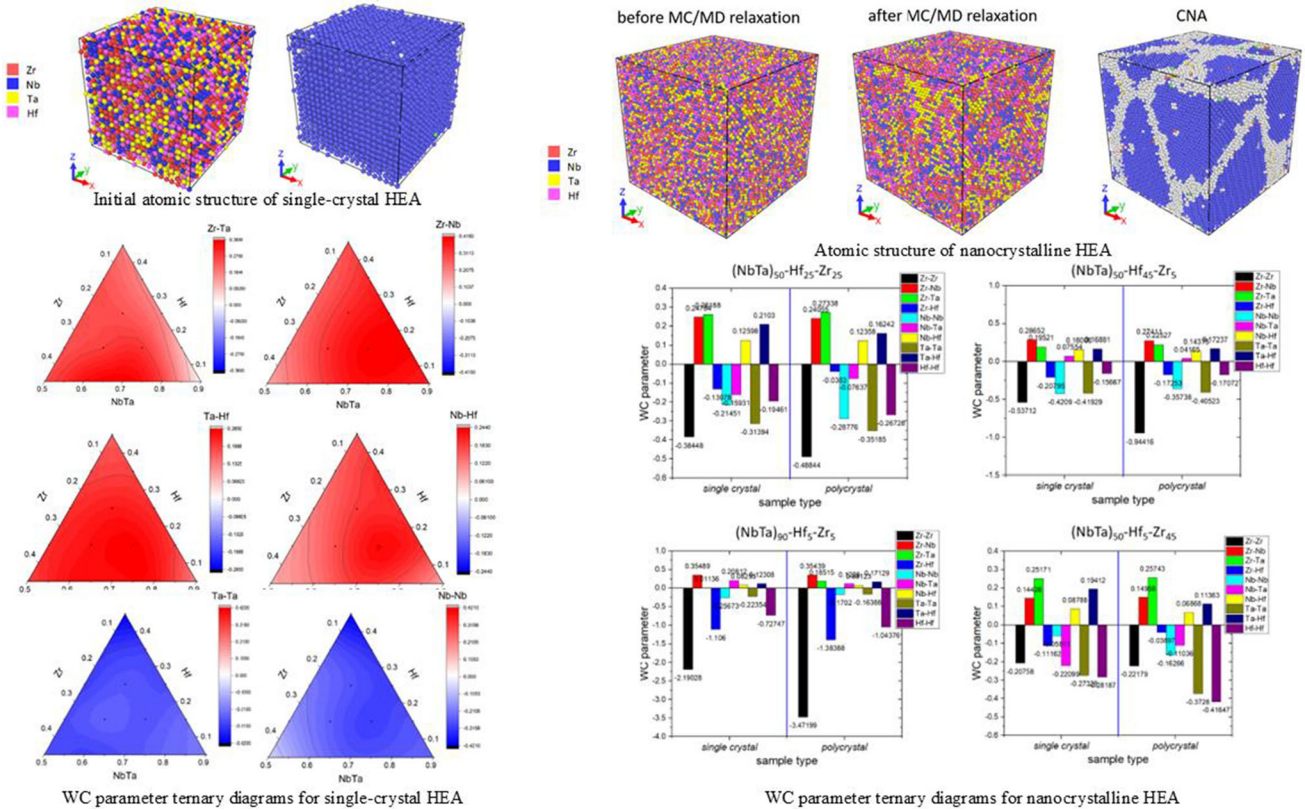

https://doi.org/10.1007/s11661-025-08003-z

I. INTRODUCTION

HIGH-ENTROPY alloys (HEAs), unlike conventional alloys composed of a single principal element,[1,2] represent an innovative class of multi-principal element materials that typically consist of four or more elements, either in equal or relatively large fractions. Comprising multiple principal elements, HEAs stabilize into face-centered cubic (fcc) or body-centered cubic (bcc) solid solutions and are commonly based on quaternary or quinary alloy systems.[3,4] Recently, these materials have garnered significant research interest due to their superior properties, which often surpass those of traditional alloys. In particular, HEAs have demonstrated outstanding mechanical properties, along with exceptional corrosion,[5] wear,[6] radiation,[7] and oxidation[8] resistance. These attributes make them highly promising for applications in both functional and structural materials. Refractory high-entropy alloys (RHEAs), a prominent class of HEA systems, are primarily composed of refractory elements including Nb, V, Zr, Ta, Hf, Mo, and W. Their remarkable resistance to softening and exceptionally high melting points render them as ideal candidates for high-temperature applications such as gas turbine blades, nuclear power stations, and aerospace.[9–13]

Compared to conventional bcc alloys, fcc alloys generally exhibit better ductility owing to multiple dislocation slip systems. However, several studies have reported that at very low temperatures, such as cryogenic conditions, bcc-structured RHEAs can demonstrate enhanced fracture resistance.[14] Among various bcc alloys, in particular, TiZrHfTa-based alloys have received great attention owing to their excellent mechanical properties and unique balance between strength and ductility,[14–16] outperforming the existing HEAs. Such alloy systems have demonstrated superior corrosion resistance,[17] biocompatibility,[18] and hydrogen storage capabilities.[19,20] These characteristics make such alloys highly suitable for structural applications across the biomedical, aerospace, automotive, and energy industries. Among many, the equiatomic HfNbTaTiZr alloy, also known as the Senkov alloy, has been one of the most investigated examples.[21]

Generally, the HEAs are assumed to exhibit a random elemental distribution to maximize their configurational entropy,[22] which is their signature effect. The high configurational entropy promotes the formation of a stable single solid solution without chemical segregation and the formation of intermetallic compounds. However, recent studies[23–25] indicate that this assumption does not always hold and provide strong evidence of

chemical short-range ordering (SRO) in HEAs. This local ordering influences the nucleation and mobility of dislocations, thereby significantly altering the mechanical properties of the alloys.[26–29] Also, the grain boundary (GB) segregation and formation of intermetallic phases through local ordering are believed to significantly influence the deformation mechanisms of HEAs. Chemical ordering can result in reduced stacking fault energy (SFE), which in turn can induce twinning and phase transformation resulting in additional hardening.[30] Ma *et al.*[31] believed that lattice distortion and chemical SRO contribute to the unconventional behavior of dislocation slip in HEAs. Chen *et al.*[32] proposed that SRO in CoCuFeNiPd influenced phase stability, and the interplay between phase tendencies and other material properties contributed to the enhanced strength and toughness of the alloy. Reportedly, Jian *et al.*[33] argued that the atomic clusters result in enhanced nucleation strain of Shockley incomplete dislocation, thereby increasing the yield strength of the material. In short, SRO is widely regarded as a fundamental characteristic of HEAs, and optimizing chemical SRO in multi-principal element systems is crucial for achieving ideal mechanical properties. However, it is noted that the studies on SRO have predominantly focused on equiatomic compositions CrFeCoNiPd,[23] FeCoNiCuPb,[26,32] NbMoTaW,[34] and ZrNbHfTa,[35] leaving its effects in non-equiatomic HEAs relatively unexplored.

Atomistic simulation methods have gained wide popularity in investigating the deformation evolution in alloys. To better understand the deformation mechanisms in HEAs, numerous molecular dynamics (MD) studies have been conducted, focusing on aspects such as SFE,[36,37] compositional effects,[38] mechanical properties,[39,40] defect interactions,[41] and phase transformations.[42] Using MD simulations, Liu *et al.*[43] conducted indentation studies on bcc HEAs, including a non-equiatomic Hf–Ta–Ti–Zr. They reported the phase transformation from bcc to hexagonal close-packed (hcp) as the primary mechanism of plastic deformation. Theoretical studies have predicted that such phase transformations play a crucial role in TiZrNbHfTa-based alloys. HEAs.[44] Chen *et al.*[45] investigated equiatomic HfNbTaZr alloys, which are compositionally similar to the Senkov alloy but lack the Ti component. Their study highlights the significance of incorporating short-range order in understanding the material's behavior. Liu *et al.*[46] conducted a study on a TaTiZrV alloy using a relatively small sample of fewer than one million atoms, with a focus on the initial stages of plastic deformation and dislocation nucleation.

Since the chemical SRO occurs at the atomic scale, MD simulations in combination with Monte Carlo (MC) technique[47–50] provide an effective means to characterize SRO in HEAs and unveil its correlation with mechanical properties. Recently, numerous studies have integrated MD and MC simulations to investigate the evolution of chemical SRO and its influence on deformation mechanisms at the atomic scale in multi-principal element alloys.[26,35,51] In other investigations, using the method, it was revealed that for the nanocrystalline (NC) alloys, SRO could suppress the inverse Hall–Petch effect,[52] alter SFE,[53] and help explain the simultaneous enhancement of strength and ductility.[32] Recent investigations indicate that there exists a strong interaction between GBs and SRO in polycrystalline HEAs, with GB segregation playing a crucial role in determining the degree of SRO within the crystal.[52,54] Li *et al.*[55] recently conducted a theoretical study on polycrystalline NbMoTaW-based HEAs, identifying both GB segregation and SRO within the crystal structure. Mantha *et al.*[54] experimentally investigated polycrystalline CoCuFeMnNi HEAs and observed Mn and Ni segregation at GBs, along with the formation of B2-ordered structures within the crystals. GB segregation, the accumulation of solute atoms at GBs, is an effective mechanism for inhibiting grain growth in polycrystalline materials.[56,57] Additionally, the segregation can alter elemental distribution within the grain interior, thereby affecting the formation of SRO structures.[55] The complex interplay between GB segregation and SRO remains still unclear, which hinders the rational design of HEAs.

This research aims to systematically investigate the effects of chemical composition and GB networks on SRO in NbTaHfZr HEAs using combined MC and MD simulations. The study focuses on the effects of chemical composition on SRO during material relaxation by employing MC/MD modeling on single-crystal samples to explore the effect of different elemental combinations on atomic clustering and local chemical ordering. Additionally, this study examines the impact of GB networks on SRO in NC HEAs by analyzing the influence of GBs on SRO and lattice stability across four different compositions. Furthermore, it investigates the effects of SRO on the high-temperature tensile deformation behavior of these four NC alloys by comparing corresponding results for relaxed and non-relaxed materials. This paper is organized as follows. Section II presents the description of the alloy compositions of single-crystal and NC HEAs, along with the details of the MD/MC simulations. Section III presents the findings on SRO in single-crystal and NC alloys, in addition to the deformation behavior of NC alloys, followed by discussions presented in Section IV. Finally, the conclusions are drawn in Section V.

II. SIMULATION MODEL AND METHOD

A. *Computational Cells and Alloy Compositions*

To study SRO in HEAs, two different computational cells of cubic shape are considered, namely, the single-crystal model (Figure 1) and the polycrystalline sample with nano-sized grains (Figure 2). The Single-crystal computational cell of HEAs $(NbTa)_x$–Hf_y–Zr_z ($x = 100–y–z$) consists of ~ 14,000 atoms. In this case, the composition of Hf and Zr (y and z, respectively) in considered alloys can vary from 5 to 45 at. pct, while the composition of NbTa changes from 50 to 90 at. pct (*i.e.*, from 25 and 45 at. pct for each element type) with the composition step of 5 at. pct. Note that

the proportion of Nb and Ta in alloys is always kept fixed at 1:1. Thus, a total of 45 different alloy compositions are considered. These single-crystal alloys are generated using Atomsk software.[58]

As the relaxation process, discussed in the subsequent section, in the case of the NC sample consisting of ~ 102,000 atoms, is computationally expensive, only four different compositions are considered. One of them is equiatomic, while the other three with extreme compositions, namely $(NbTa)_{50}$–Hf_5–Zr_{45}, $(NbTa)_{50}$–Hf_{45}–Zr_5, and $(NbTa)_{90}$–Hf_5–Zr_5. The polycrystalline samples are constructed using the Voronoi procedure implemented in the Atomsk software. The samples have dimensions of $13 \times 13 \times 13$ nm^3.

B. *Simulation Setup*

For the investigation purpose, at the initial state, constituent atoms were distributed randomly inside the HEAs. To obtain a more realistic steady state that takes diffusion into account and possible SRO, combined MC/MD simulations were performed. SRO is studied for both single-crystal and NC samples described earlier, while its effect on the deformation behavior during high-temperature tensile loading is considered only for the selected four different NC HEAs. Interatomic forces in the considered materials are described by the modified embedded atom method potential developed by Huang *et al.*[35]

The MC/MD simulation of material relaxation includes simultaneous atomic swapping based on the MC approach and the MD thermalization at 1000 K by integrating the classical equations of motion. Before such relaxation, the material systems under investigation are subjected to energy minimization using the conjugate gradient method and further equilibrated within 50 ps, keeping all the pressure components at 0 Pa and the temperature at 1000 K by using the isothermal–isobaric (NPT) ensemble. In the study, the simulation timestep is set to 1 fs, and the periodic boundary conditions are imposed along the orthogonal x, y, and z axes. Swapping of one atom type with an atom of another type is realized using the widely accepted MC procedure that follows the Metropolis acceptance criterion,[59] which determines the probability of atom exchange at a given temperature. As per this approach, the MC swap takes place if the alloy energy E after the $(i + 1)$th atom exchange is lower than the energy at the previous attempt i. On the contrary, the swap is accepted with a probability defined as follows:

$$P = \exp(-(E(i+1) - E(i))/kT),$$

where T is the given temperature and k is the Boltzmann constant. Within one timestep, only one swap is realized, and the kinetic energy is kept unchanged before and after such an atom exchange.

For single-crystal samples, the MC/MD simulations are performed within 80 relaxation cycles. Each cycle includes 12,000 MC swaps followed by MD equilibration within 5000 fs. A total of 960,000 swaps are performed for each composition. Same as for the single-crystal case, for the NC samples, the MC/MD simulations are performed at 1000 K but only for 100 relaxation cycles, as the larger sample requires more atomic swaps to reach the steady state condition (Figure 3). For each NC alloy, 1,200,000 swaps are performed during the relaxation procedure. It is noted that the relaxation process was considered converged once the change in potential energy per atom between successive MC/MD cycles dropped below ~ 1×10 3 eV/atom.

The chemical affinity between a pair of atoms of the HEAs subjected to the MC/MD relaxation through atomic swapping is assessed by calculating the Warren–Cowley (WC) parameter as follows:

$$\text{WC parameter} = 1 - Z_{mn}/(\chi_n Z_m),$$

where χ_n is the atomic fraction of n atoms in the alloy, Z_{mn} is the number of n atoms at the first neighbor shell of m atoms, and Z_m is the total number of atoms at the first neighbor shell of m atoms.[60] When the WC parameter is 0, the m and n atoms are distributed randomly; if this value is positive, they tend to be far from each other. On the contrary, when the WC parameter is negative, the formation of clusters or compounds of m and n atoms with chemical bonds between them is more likely.

Tensile deformation tests of the NC HEAs without a preliminary MC/MD relaxation procedure, when the constituent atoms are distributed randomly within the structure, and after the hybrid MC/MD simulation described earlier, are conducted at 1000 K up to a strain of 20 pct. The samples are subjected to uniaxial loading along the x-axis (see Figure 2) in the NPT ensemble with a strain rate of 5×10^9 s^{-1}. Periodic boundary conditions are imposed along the x, y, and z axes. Both the MC and MD simulations are conducted using the large-scale atomic/molecular massively parallel simulator (LAMMPS).[61] The atomic structure visualization and its analysis are performed with the help of the OVITO software.[62]

III. RESULTS

A. *SRO in the Single-Crystalline and NC Samples*

The calculation of WC parameters for different pairs of elements in the alloy is an effective method to quantify the SRO because the values obtained directly correlate with the atomic order of the considered structure. Figure 4 presents the WC parameter ternary diagrams for single-crystal alloys, the simulated compositions highlighted by black dots, demonstrating that during the relaxation of the single-crystal models through the MC/MD simulation, elements of the atomic pairs Zr–Ta, Zr–Nb, Ta–Hf, Nb–Hf do not tend to form chemical bonds with each other (two upper rows), while atoms of Ta and Nb demonstrate relatively high tendency for bonding with the atoms of same element type forming corresponding clusters (lower row). The former case is characterized by positive WC parameters (red color in Figure 4), while in the latter one, the WC

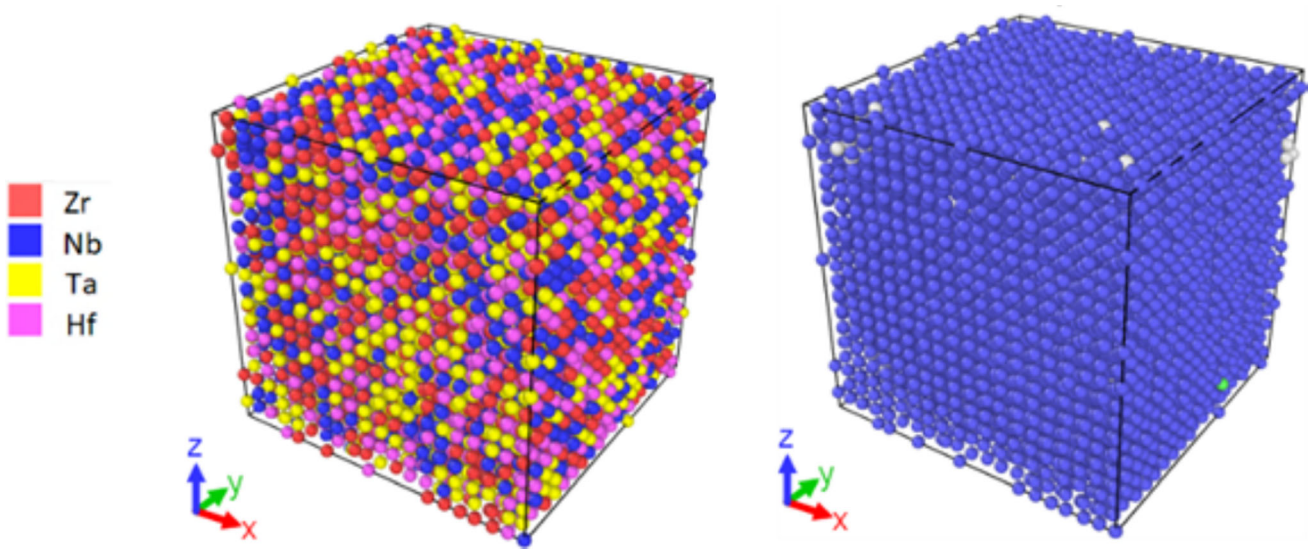

Fig. 1—Typical initial atomic structure of single-crystal HEA (example is given for $(NbTa)_{50}$–Zr_{25}–Hf_{25}) with atoms of different types randomly distributed in it (on the left). The common neighbor analysis (CNA) of the corresponding alloy, where atoms colored in blue form a bcc structure (on the right) (Color figure online).

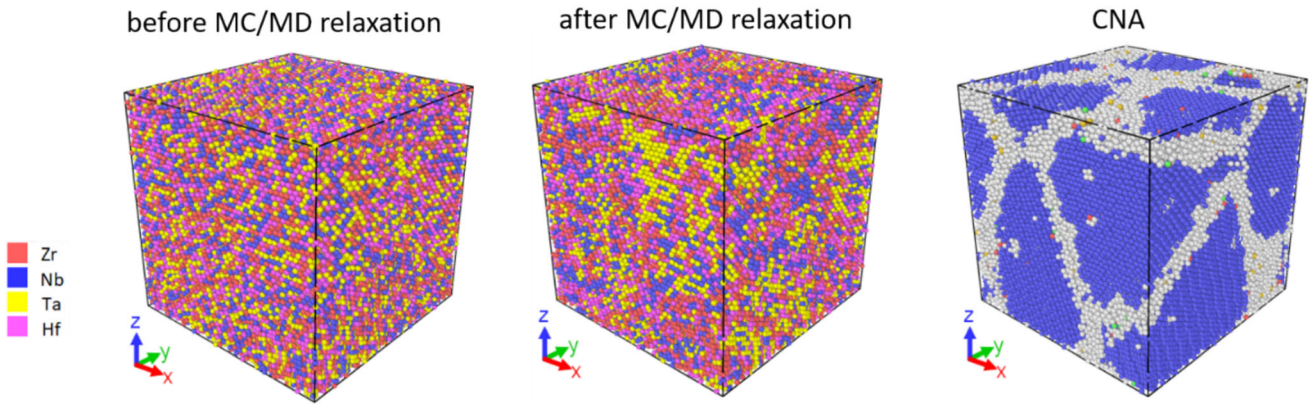

Fig. 2—Atomic structure of NC HEA $(NbTa)_{50}$–Hf_{25}–Zr_{25} before and after the MC/MD relaxation. For the CNA structure (on the right), blue atoms correspond to the initial bcc structure, and gray atoms correspond to the disordered areas, mainly GBs.

parameters are negative (blue color in Figure 4). For the mentioned atomic pairs, the change in alloy composition affects the WC parameter insignificantly.

At the same time, for the other atomic pairs, including Zr–Zr, Hf–Hf, Zr–Hf, and Nb–Ta, the composition significantly affects the ability for clustering of the corresponding atoms [Figure 5(a)]. It is observed that the elements in the pairs Zr–Zr, Hf–Hf, and Zr–Hf tend to form chemical bonds with each other at higher content of Nb and Ta in the alloys. At the same time, at a lower content of the latter elements, the WC parameter for these pairs increases, indicating a reduced ability to form clusters. It is also evident from Figure 5(b) that clusters of the ordered NbTa structure are more readily formed as the content of Nb and Ta atoms in the HEAs decreases.

Figure 6 shows WC parameter diagrams obtained after the MC/MD relaxation procedure for the atomic pairs of the four NC alloys (Figure 2), namely $(NbTa)_{50}$–Hf_{25}–Zr_{25}, $(NbTa)_{50}$–Hf_5–Zr_{45}, $(NbTa)_{90}$–Hf_5–Zr_5, and $(NbTa)_{50}$–Hf_{45}–Zr_5 and compares the values for corresponding single-crystal alloys (Figure 1). Note that in the case of polycrystals, the WC parameters are calculated only for the areas inside grains and do not consider GB regions. It is observed that the WC parameters for some atomic pairs differ significantly between the single-crystal and NC samples. In particular, it is evident for the atomic pairs Zr–Zr, Nb–Nb, Ta–Ta, Nb–Ta, and Hf–Hf that the values become more negative for samples having a GB network. A similar trend is observed for the pair Ta–Hf, for which the WC parameter decreases but remains positive. Such a difference is due to the presence of GBs in the NC materials.

To understand the effect of the GB network on SRO, further, the change in composition inside grains and in GB areas is analyzed for the four NC alloys during their MC/MD relaxation. Figure 7 demonstrates the variation in concentration of the constituent elements of these HEAs with relaxation cycles. The relaxation process was

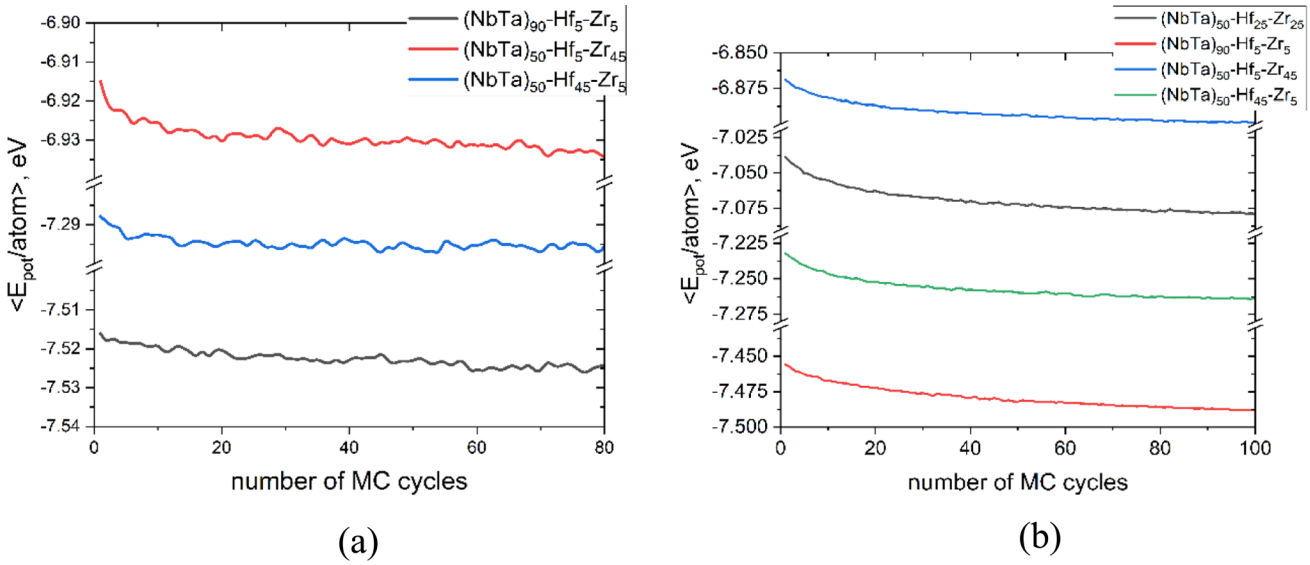

Fig. 3—Decrease in the average potential energy per atom with cycles of the MC/MD relaxation for (*a*) three different examples of single-crystal HEAs and (*b*) four NC materials.

considered to be converged once the change in composition between the last few steps drops below 0.1 pct for each element. In the equiatomic alloy [Figure 7(a)], with an increase in the number of MC/MD cycles, the content of Ta increases significantly up to 33 at. pct inside the grains while decreasing to 12.5 at. pct in the GB regions. On the contrary, the content of Nb, Hf, and especially Zr, gradually increases in GBs and decreases inside grains. The same trend for the elements can be seen for the other three considered alloys; however, the change in composition before and after the relaxation is not as pronounced as for the equiatomic sample [see Figures 7(b) through (d)]. It can be concluded that the relaxation process leads to the depletion of the GBs in the NC alloys, especially $(NbTa)_{50}$–Hf_{25}–Zr_{25}, with the Ta atoms, while some GB segregation of Zr, Nb, and Hf atoms takes place.

B. *Deformation Behavior of NC Alloys*

Further, the tensile deformation behavior of the polycrystalline materials is studied before and after their MC/MD relaxation under high-temperature conditions. As evident from the stress–strain curves plotted in Figure 8, for all the considered alloy compositions, the yield strength for the relaxed alloys is observed to be much higher than that obtained for the corresponding materials before the MC/MD atom swapping process. Especially, it is evident for the equiatomic composition and $(NbTa)_{50}$–Hf_{45}–Zr_5, where the content of Hf is relatively higher [Figures 8(a) and (c)]. However, unlike the other compositions, with further deformation of $(NbTa)_{50}$–Hf_{45}–Zr_5, the stresses are observed to be higher in the non-relaxed material state.

Table I presents the tensile test results, namely lists the yield strength and corresponding yield strain for the NC alloys before and after the MC/MD relaxation. As observed, within the HEAs, $(NbTa)_{90}$–Hf_5–Zr_5 subjected to the MC/MD relaxation demonstrates the highest strength, while $(NbTa)_{50}$–Hf_{45}–Zr_5 without preliminary relaxation shows the lowest yield strength.

Strain hardening reflects the ability of a material to strengthen in response to plastic deformation when it is strained beyond the yield point. In Figure 9, the dependence of strain hardening rate on tensile strain is presented for the HEAs. Here, the strengthening of the material is observed in the regions, where the curves are above the blue dashed lines corresponding to the strain hardening rate of 0 GPa, but without considering the first sharp decrease from positive values. It can be seen that the hardening rate of $(NbTa)_{50}$–Hf_{45}–Zr_5 without preliminary MC/MD relaxation (black line) is found to be the highest among all considered material systems; it reaches 46.16 GPa (Figure 9). However, after the MC/MD atomic swapping, it decreases significantly, and the strengthening starts only around $\varepsilon_{xx} = 0.07$. Similar behavior is also observed for the equiatomic alloy; however, the strain hardening rate in the case of the non-relaxed alloy does not reach such a high value (15.64 GPa over 46.16 GPa). As for $(NbTa)_{90}$–Hf_5–Zr_5, unlike the non-relaxed material, the strengthening of the alloy after the MC/MD relaxation can hardly be observed. It is noted that $(NbTa)_{50}$–Hf_5–Zr_{45} is the only composition where the strain hardening rate of the ordered alloy is slightly higher than that of the corresponding alloy without the MC/MD relaxation. At $\varepsilon_{xx} = 0.12$, it reaches 19.44 GPa, but the hardening here occurs only over a relatively short strain interval.

IV. DISCUSSION

A. *Effect of GBs on SRO Process*

Figure 6 demonstrates that the WC parameters of the Nb–Ta pair for the alloys $(NbTa)_{50}$–Hf_{25}–Zr_{25} and $(NbTa)_{90}$–Hf_5–Zr_5 differ significantly; at a lower content

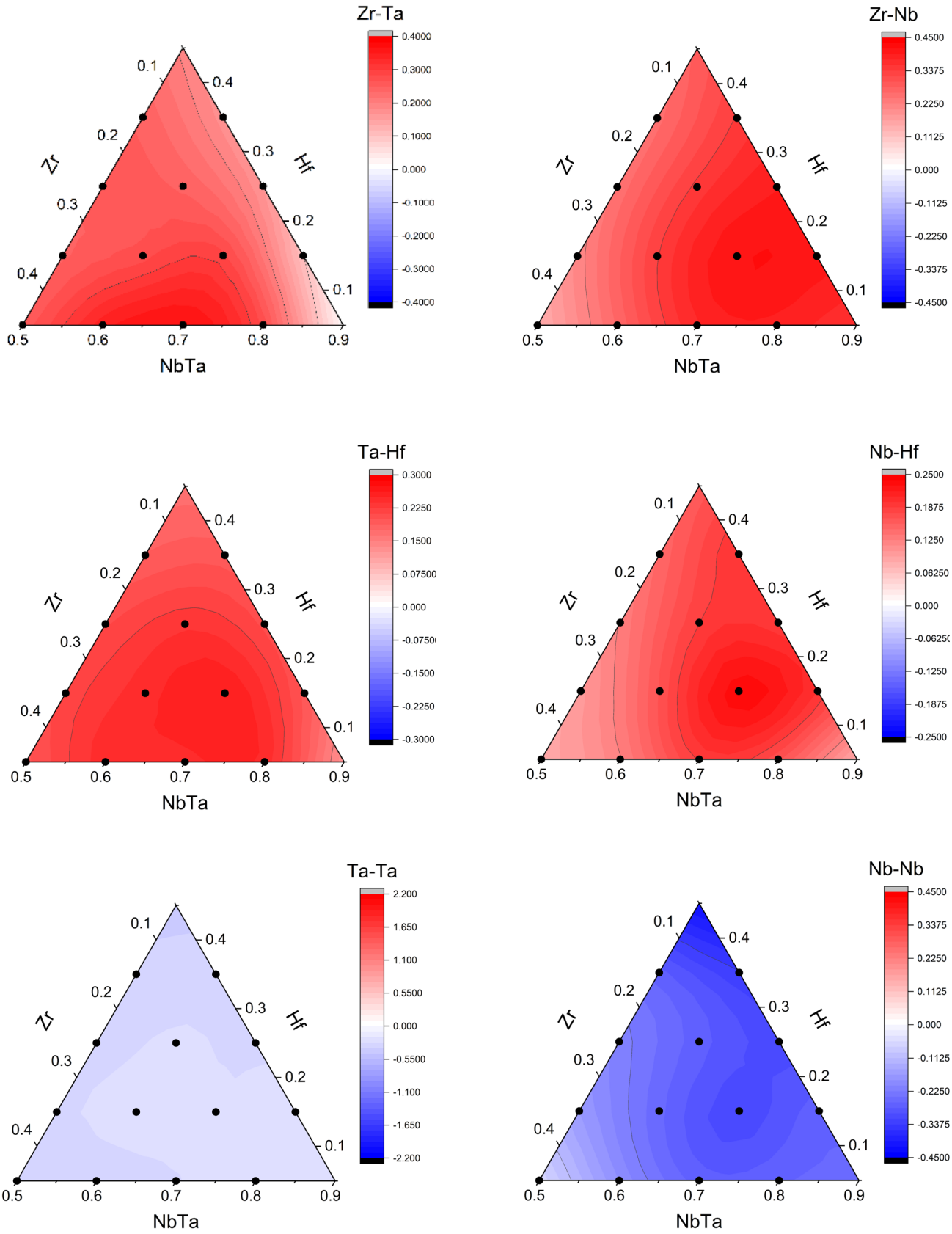

Fig. 4—WC parameter ternary diagrams for different atomic pairs after the MC/MD relaxation procedure of the single-crystal HEAs, depending on the alloy composition (Color figure online).

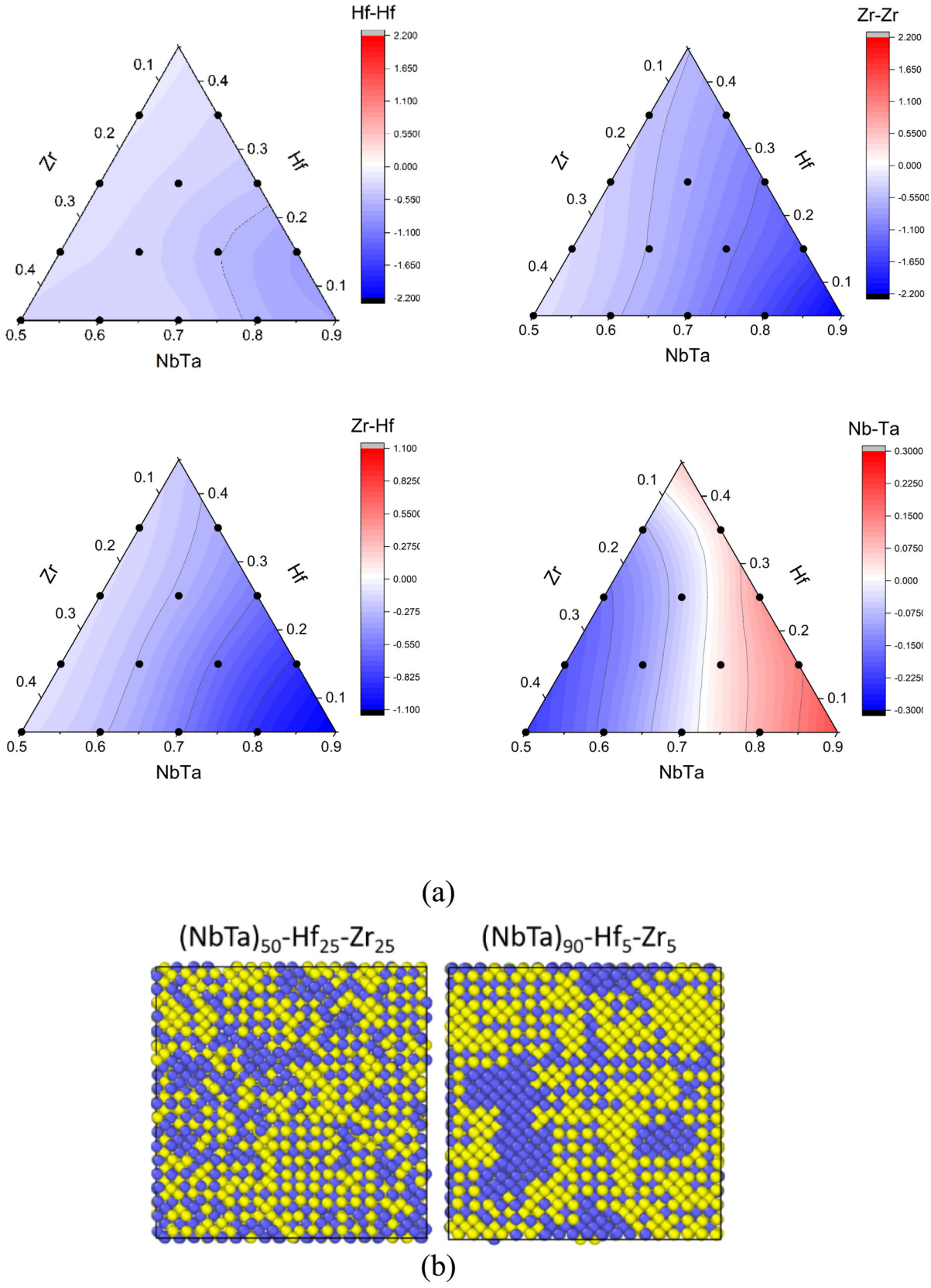

Fig. 5—(*a*) WC parameter ternary diagrams for Zr–Zr, Hf–Hf, Zr–Hf, and Nb–Ta atomic pairs after the MC/MD relaxation procedure of the single-crystal HEAs; and (*b*) Atomic distribution for Nb (blue color) and Ta (yellow color) in HEAs $NbTa_{50}Hf_{25}Zr_{25}$ and $NbTa_{90}Hf_5Zr_5$ after the MC/MD relaxation. In (b), the Hf and Zr atoms are removed for better visualization of SRO areas (Color figure online).

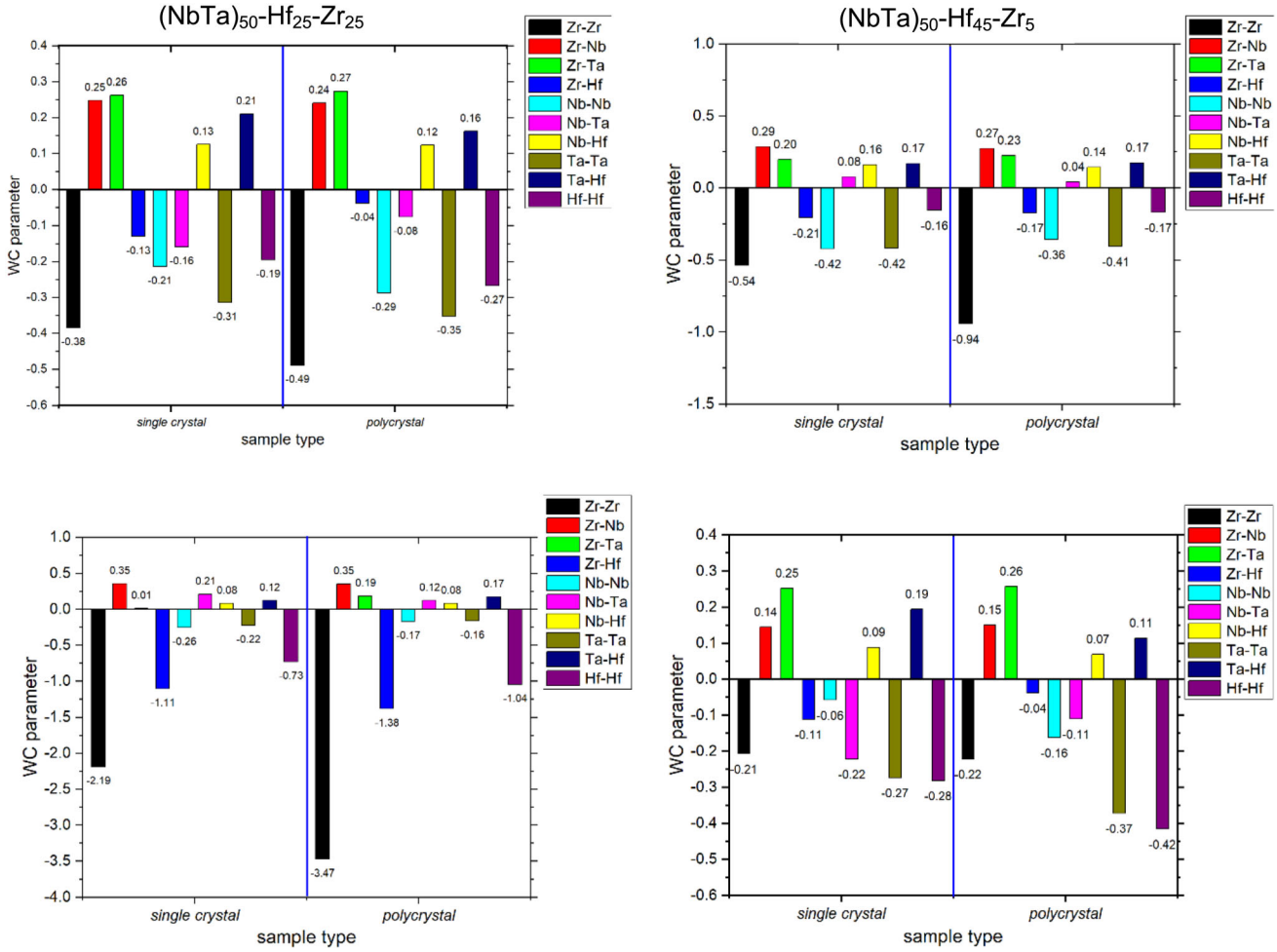

Fig. 6—WC parameters for single crystals and the polycrystals (inside grains) after the MC/MD relaxation.

of Nb and Ta, the WC parameter decreases. This finding is in agreement with the conclusions reported by Jarlov *et al.*[63], where the authors claimed that the tendency to form ordered clusters increases with the decrease in the content of elements forming such clusters. The results show that Nb and Ta, as well as Zr and Hf atoms, tend to form ordered clusters with a B2 superstructure. Radial distribution functions (RDFs) for the atomic pairs Nb–Ta and Zr–Hf in the relaxed single-crystal HEAs $(NbTa)_{90}$–Hf_5–Zr_5 and $(NbTa)_{50}$–Hf_{25}–Zr_{25} are compared with those for NbTa and ZrHf with B2 structure (Figure 10). Despite the higher content of Nb and Ta in HEA $(NbTa)_{90}$–Hf_5–Zr_5, the intensity of the peak at position $r = 5.6$ Å associated with the presence of the B2 lattice is lower than that of the equiatomic alloy. This corroborates the fact that with a decrease in the content of the clustering element, its tendency to form corresponding ordered structures increases.

Thus, the GB network significantly affects the distribution of the elements in the alloys, and as a result, the chemical composition within the structure also gets altered. The chemical composition analysis shows that during the MC/MD atomic swapping, the atoms of Zr, Nb, and Hf segregate at GBs, while Ta prefers to remain within the grains. In fact, the atomic radius of Hf is the biggest within the alloy's constituent elements, and to decrease lattice distortion caused by such big atoms, they tend to occupy positions at GB regions having free volume. At the same time, the chemical affinity of Ta to other elements, especially to Hf and Zr, is very low, whereas Hf and Zr easily form chemical bonds with each other (Figure 6). This leads to the depletion of GBs with Ta atoms and their enrichment with the other elements (Figure 7).

Enrichment of grains with Ta atoms results in an increased WC parameter for the Nb–Ta atomic pair compared to the single-crystal alloys, while for the Nb–Nb, Zr–Zr, and Hf–Hf atomic pairs, the situation is opposite (Figure 6). Within the NC alloys, the WC parameters of Nb–Ta and Zr–Hf are more negative in the case of HEAs $(NbTa)_{50}$–Hf_5–Zr_{45} (− 0.11036) and $(NbTa)_{90}$–Hf_5–Zr_5 (− 3.4720), respectively. Due to a decrease in Zr and Hf content inside grains of $(NbTa)_{90}$–Hf_5–Zr_5 upon the MC/MD relaxation, the chemical affinity between them becomes slightly higher compared to that of the single-crystal sample.

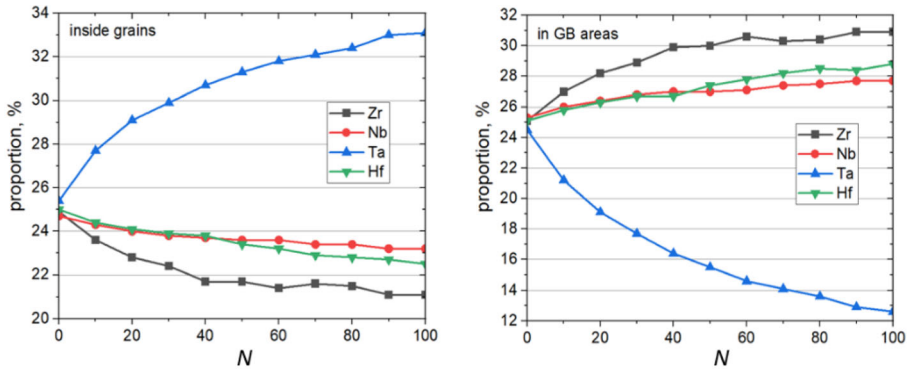

(a)

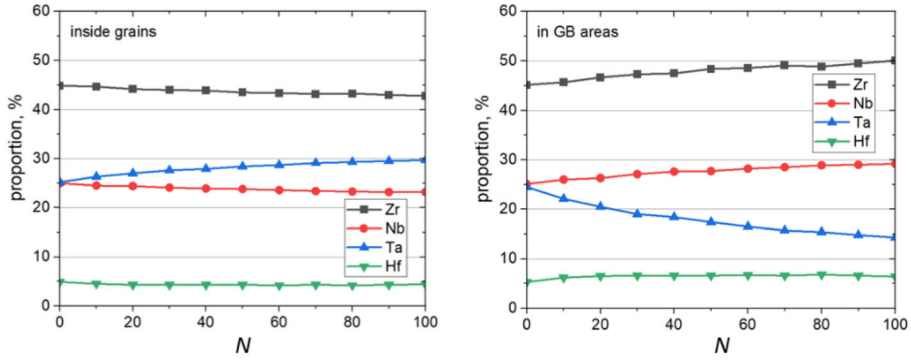

(b)

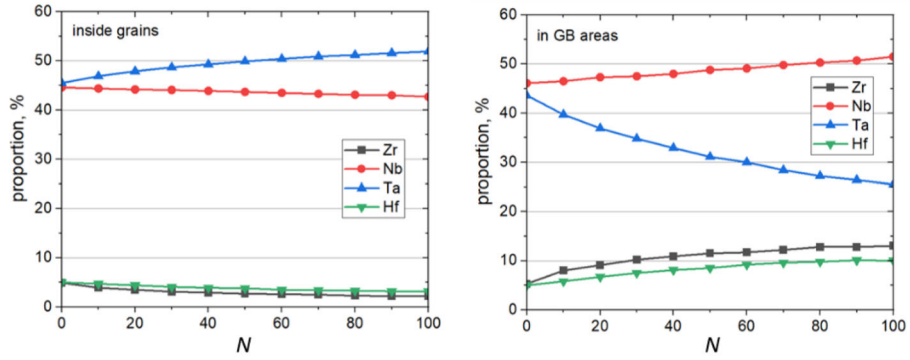

(c)

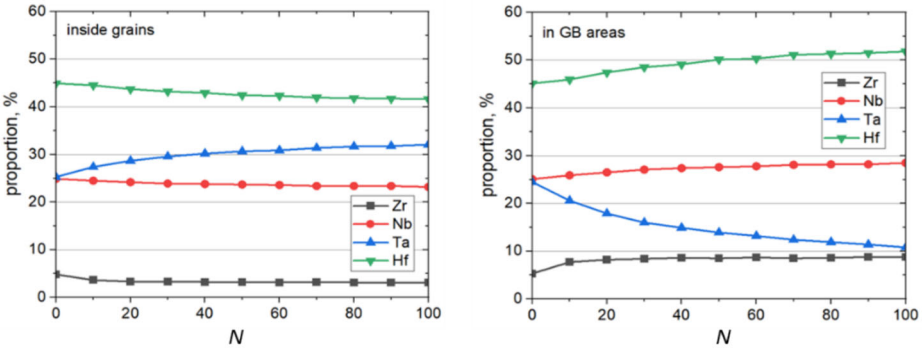

(d)

Fig. 7—Change in composition inside grains and in GB areas for the NC HEAs with cycles of the MC/MD relaxation (N) for (*a*) $(NbTa)_{50}$–Hf_{25}–Zr_{25}, (*b*) $(NbTa)_{50}$–Hf_5–Zr_{45}, (*c*) $(NbTa)_{90}$–Hf_5–Zr_5, and (*d*) $(NbTa)_{50}$–Hf_{45}–Zr_5.

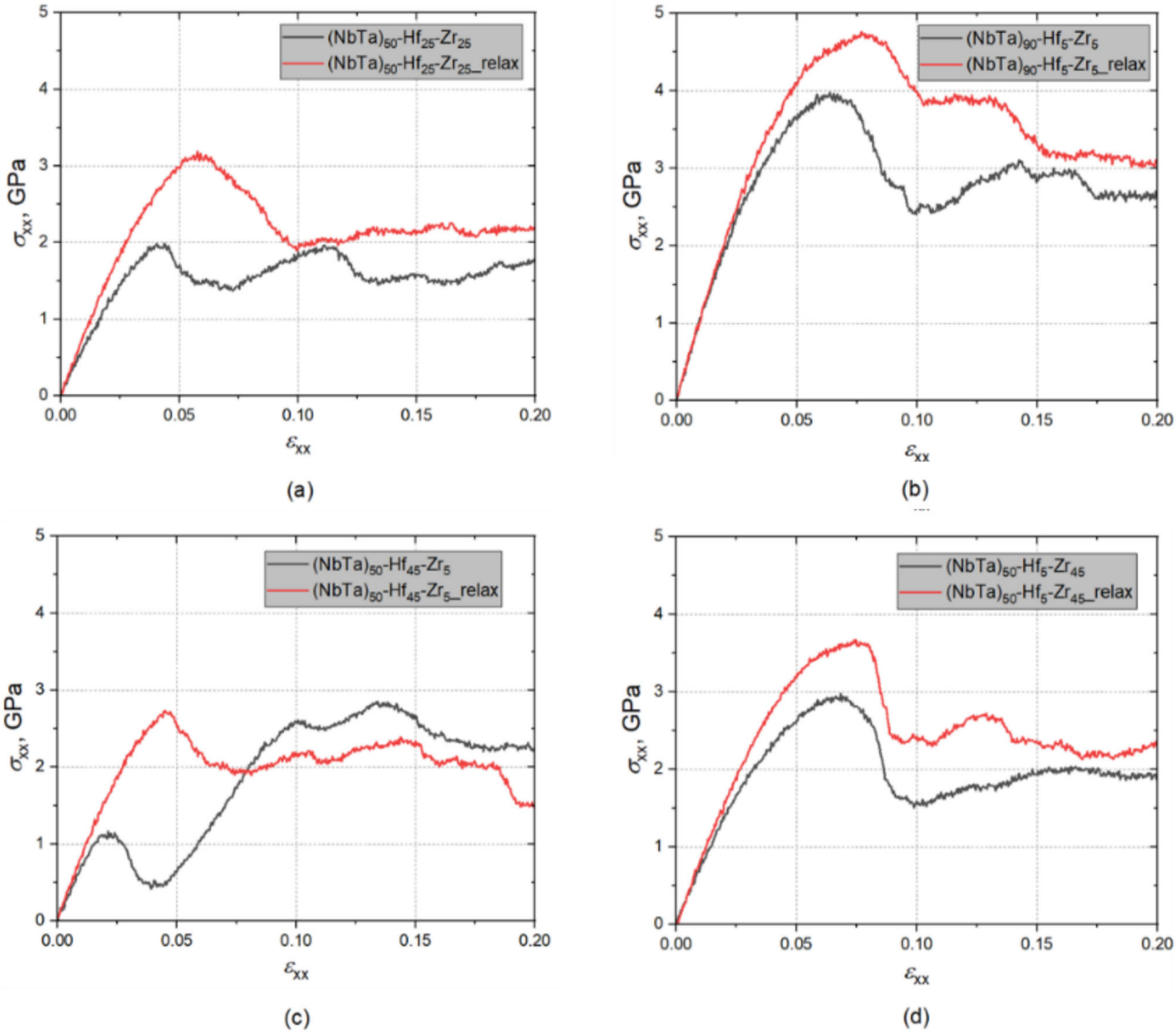

Fig. 8—Tensile deformation stress–strain curves for HEAs (*a*) $(NbTa)_{50}$–Hf_{25}–Zr_{25}, (*b*) $(NbTa)_{90}$–Hf_5–Zr_5, (*c*) $(NbTa)_{50}$–Hf_{45}–Zr_5, and (*d*) $(NbTa)_{50}$–Hf_5–Zr_{45} before and after the MC/MD relaxation.

B. *Chemical Composition Effect on Deformation Behavior*

As can be seen from snippets of deformed structures of the NC HEAs (Figure 11) and phase evolution analysis (Figure 12), the materials with higher content of Hf, namely $(NbTa)_{50}$–Hf_{25}–Zr_{25} and $(NbTa)_{50}$–Hf_{45}–Zr_5, undergo bcc-to-hcp phase transformation during tension at 1000 K, and one can conclude that the stress-induced phase transition is the main deformation mechanism for them. For these two HEAs, as well as for $(NbTa)_{90}$–Hf_5–Zr_5, especially for the ordered one, the areas of fcc phase can also be detected.

According to the phase evolution analysis, for the relaxed $(NbTa)_{50}$–Hf_{45}–Zr_5 alloy, the bcc-to-fcc and hcp phase transition starts at $\varepsilon_{xx} \approx 0.015$, while for the corresponding non-relaxed alloy and the equiatomic one subjected to the MC/MD atomic swapping, it happens only at $\varepsilon_{xx} \approx 0.04$. The addition of Hf decreases the stability of the bcc structure in multi-component alloys, which was also reported earlier.[30,64] This can explain the reduced yield strength for these alloys compared to the other studied NC materials (Table I). However, in the case of the equiatomic alloy with an ordered structure, the phase transformation can hardly be observed (Figures 11 and 12). The change of alloy composition inside grains retards the phase transition process; the amount of Hf inside grains decreases, while the content of Ta increases significantly (Figure 7). It is known that such elements as Nb and Ta are good bcc structure stabilizers.[64,65] During tension, the fraction of disordered structure gradually increases for all the compositions; however, for $(NbTa)_{50}$–Hf_{45}–Zr_5, where the accommodation process occurs through a phase transition, it is not so obvious. The deformation process in the other materials considered is primarily associated

with the dislocation sliding and accompanied by the twins and shear band formation (Figure 11).

Figure 13 shows the results of the dislocation structure evolution analysis. The total dislocation length for the HEA $(NbTa)_{50}$–Hf_{45}–Zr_5, regardless of whether there is preliminary relaxation through the MC/MD atomic swapping, increases with loading. In general, the phase transition in the HEAs is accompanied by the formation of dislocations, preferably 1/6<112> Shockley partials and the 1/3<100> Hirth dislocations in the fcc phase and 1/3<1-100> dislocations in the hcp structure. The slope of the curves indicates that the accumulation of dislocations in the non-relaxed alloy happens faster and at a lower deformation level. This is the reason for the high strain hardening rate compared to that of the alloy with the ordered structure and having a much higher yield strength value (Figure 9). It should be noted that boundaries between newly formed phase domains serve as dislocation nucleation sites, thereby promoting stacking fault formation. However, in the non-relaxed sample, by ~ 10 pct deformation, the accumulation of a high defect density hinders further dislocation generation (Figure 13), leading to a saturation of the flow stress.

In the case of the equiatomic composition, noticeable accumulation of dislocations occurs only for the alloy without the MC/MD relaxation. The results prove that SRO in the material slows down the dislocation generation and, as a result, decreases the strain hardening rate.

As for the other materials with a lower content of Hf, the increase of dislocation density can hardly be seen in Figure 13. Even though the total dislocation length for them almost does not change with tensile loading, some segments of the $1/2\langle 111\rangle$ perfect screw dislocations can be found in the deformed structures. It is believed that the stacking faults and deformation twins in bcc alloys form as a result of the sliding of $1/3\langle 111\rangle$, $1/6\langle 111\rangle$, and $1/12\langle 111\rangle$ partial dislocations, which can be produced from the $1/2\langle 111\rangle$ perfect dislocations.[66]

In the relaxed Hf-rich alloy, the continuous stress-induced phase transition suppresses dislocation generation, which in turn reduces strain hardening. For alloys with lower Hf content, the MC/MD relaxation alters the grain interior composition and inhibits the bcc-to-hcp phase transition. Because dislocation activity in the stable bcc phase is restricted by the limited number of available slip systems, strain hardening becomes less pronounced in these materials (Figure 8). It is known that the chemical heterogeneity of HEAs can decrease local SFE and, as a result, lead to reduced yield strength.[63,67] As was mentioned earlier, Nb and Ta are great bcc structure stabilizers, and obviously, the high content of these elements leads to increased SFE and enhanced yield strength (Table I).

Table I. Yield Strength σ_y and Yield Strain ε_y of the HEAs Before and After the MC/MD Relaxation

	$(NbTa)_{50}$–Hf_{25}–Zr_{25}	$(NbTa)_{50}$–Hf_{25}–Zr_{25}_rel	$(NbTa)_{90}$–Hf_5–Zr_5	$(NbTa)_{90}$–Hf_5–Zr_5_rel	$(NbTa)_{50}$–Hf_{45}–Zr_5	$(NbTa)_{50}$–Hf_{45}–Zr_5_rel	$(NbTa)_{50}$–Hf_5–Zr_{45}	$(NbTa)_{50}$–Hf_5–Zr_{45}_rel
σ_y, GPa	1.978	3.190	3.946	4.711	1.121	2.701	2.945	3.668
ε_y	0.04	0.058	0.061	0.076	0.019	0.045	0.066	0.075

C. *Contribution of B2 Clusters to Material Strengthening*

Along with coherent B2 compounds of NbTa and ZrHf, after the MC/MD relaxation process, some nano-sized bcc conglomerates consisting solely of Zr, Nb, Ta, or Hf atoms can be found in the considered

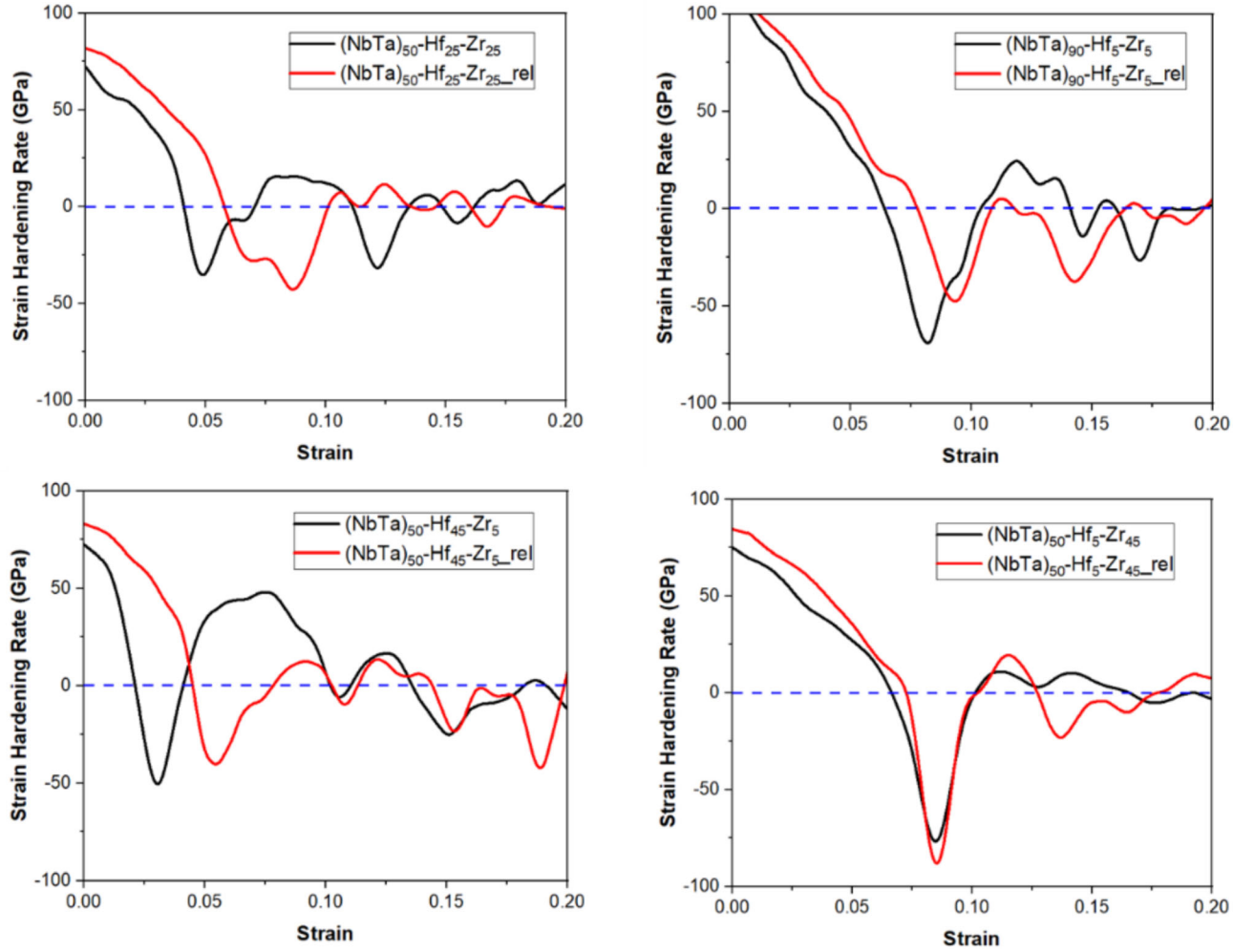

Fig. 9—Strain hardening rate as a function of strain (Color figure online).

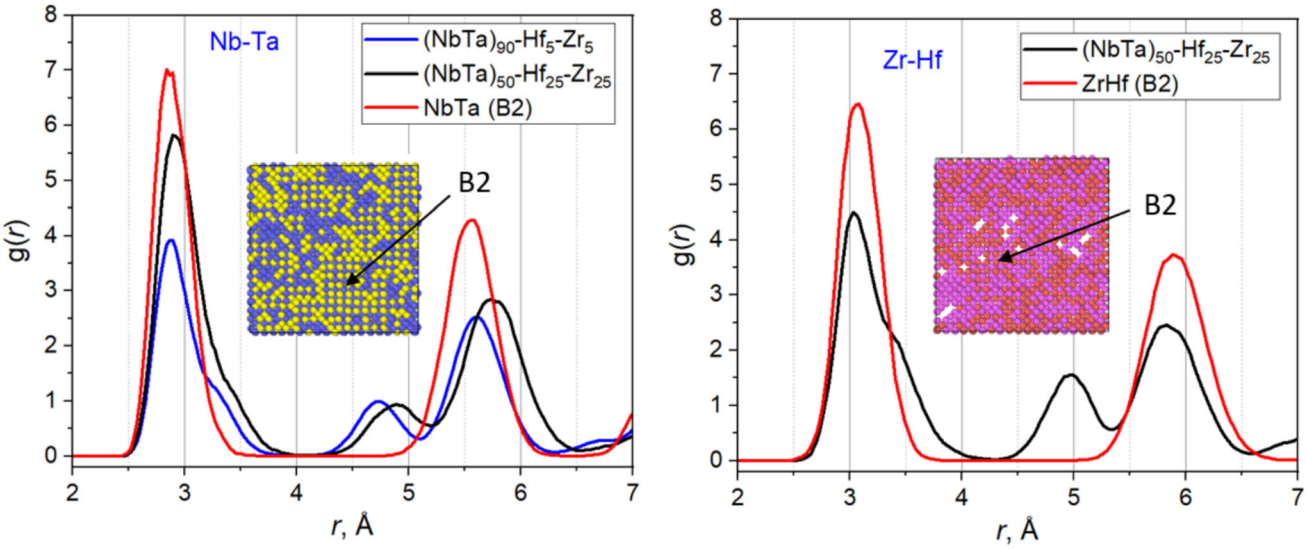

Fig. 10—RDFs for the Nb–Ta (on the left) and Zr–Hf (on the right) atomic pairs in HEAs having atoms distributed randomly within their structure in comparison with RDFs of NbTa and ZrHf compounds with B2 superstructure.

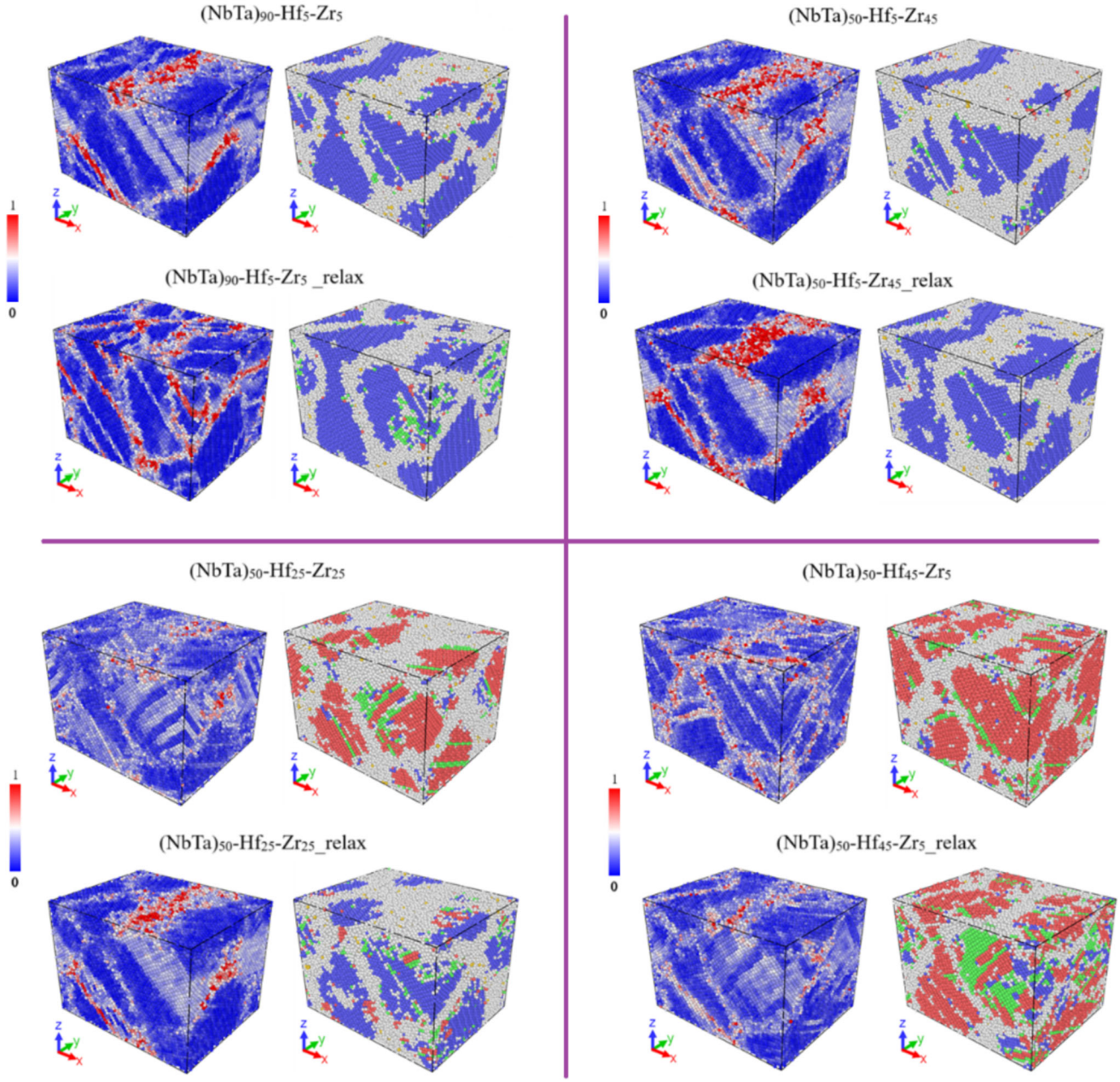

Fig. 11—Atomic structure colored based on CNA (on the right) and the corresponding von Mises shear strain distribution (on the left) of the HEAs after ε_{xx} = 0.2 tensile deformation. For the CNA structures, blue and green atoms correspond to the bcc and fcc phases, respectively. The hcp structure is shown by red atoms, while gray atoms correspond to the disordered GB areas and other lattice defects (Color figure online).

alloys. The calculated lattice parameters at 1000 K for the ZrHf and NbTa B2 compounds are 3.570 Å and 3.352 Å, respectively, while for the bcc equiatomic HEA with randomly distributed atoms, it is equal to 3.487 Å. Unlike NbTa, the B2 lattice of ZrHf, as well as bcc regions enriched with Zr or Hf, are not stable during deformation and transform easily to fcc and hcp phases.

Taking into account the chemical compositions of the alloys considered, most likely that the fraction of ZrHf-ordered particles in the materials will not be high, and, in addition, such clusters are not stable and undergo phase transition at early stages of deformation. This means that they are not able to enhance the yield strength. Therefore, further analysis is devoted to understanding the effect of NbTa coherent nanoclusters with a stable B2 structure on the deformation behavior of the HEAs.

Further, the possible strengthening effect of coherent NbTa particles was considered only for HEAs with relatively stable bcc structures during subsequent tensile deformation. For this, the uniaxial tensile deformation is conducted on single-crystalline $(NbTa)_{90}$–Hf_5–Zr_5 and $(NbTa)_{50}$–Hf_5–Zr_{45} samples with the coherent NbTa particle introduced into them (Figure 14). The

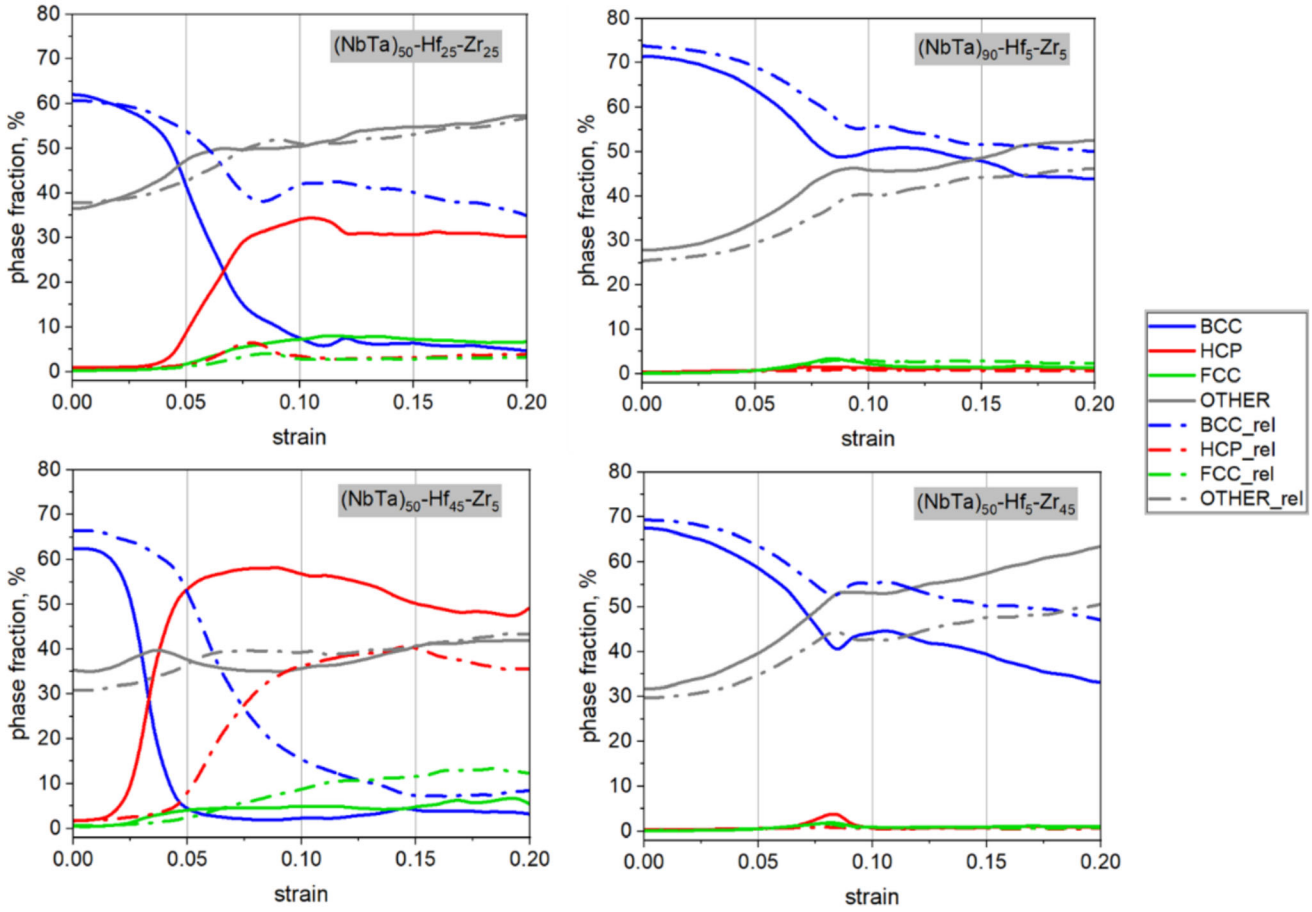

Fig. 12—Change of phase fraction in the HEAs during tensile deformation.

dimensions of the samples are 21 × 14 × 14 nm^3, while the diameter of the spherical particle is set as 6 nm. Note, atoms in the matrix surrounding the particles are distributed randomly. The same tensile deformation conditions, namely temperature, strain rate, loading direction, and boundary conditions as in the case of the NC alloy's deformation, are used.

The results of atomic strain calculation before deformation demonstrate that due to the lattice parameter mismatch of NbTa and the $(NbTa)_{50}$–Hf_5–Zr_{45} matrix, there are some elastic stresses at their interface. In the second case, the material is strained uniformly, indicating that the lattice parameters of the matrix and the particle are very close.

Upon tensile loading of the single-crystalline $(NbTa)_{50}$–Hf_5–Zr_{45}, the coherent NbTa particle endures higher stresses than the alloy matrix. This reduces the local internal stresses in the matrix, providing stress transfer strengthening. This proves that the accumulation of internal stresses in the coherent particle can inhibit the preliminary stress relaxation in the matrix. The positive influence of coherent B2 nanoparticles was recently observed experimentally by Soni *et al.*[68] They found that B2 particles in the bcc refractory $Al_{0.5}NbTa_{0.8}Ti_{1.5}V_{0.2}Zr$ HEA can provide high yield strength. The mechanism of such strengthening was also described using MD simulation in Reference 69. However, this phenomenon is not evident for the $(NbTa)_{90}$–Hf_5–Zr_5 alloy (Figure 14). This can be explained by the difference in the strength of the matrix phase surrounding the coherent particles.

Table II lists the calculated elastic moduli of four considered single-crystalline alloys with atoms distributed randomly within their structures. It is seen that $(NbTa)_{90}$–Hf_5–Zr_5 is characterized by a very high Young's modulus of 264.952 GPa, while for $(NbTa)_{50}$–Hf_5–Zr_{45}, it is lower (167.468 GPa). During tension of the latter, the particles undergo higher stresses compared to the surrounding matrix, strengthening the material through the load transfer mechanism more effectively than when we deal with a very strong $(NbTa)_{90}$–Hf_5–Zr_5 alloy.

The alloy with a high content of Zr atoms demonstrates that stress release occurs first through the fcc phase formation and stacking faults nucleation at the particle–matrix interface (Figure 14). It was also reported earlier that areas enriched with Zr can promote bcc-to-fcc transition that, at the same time, is

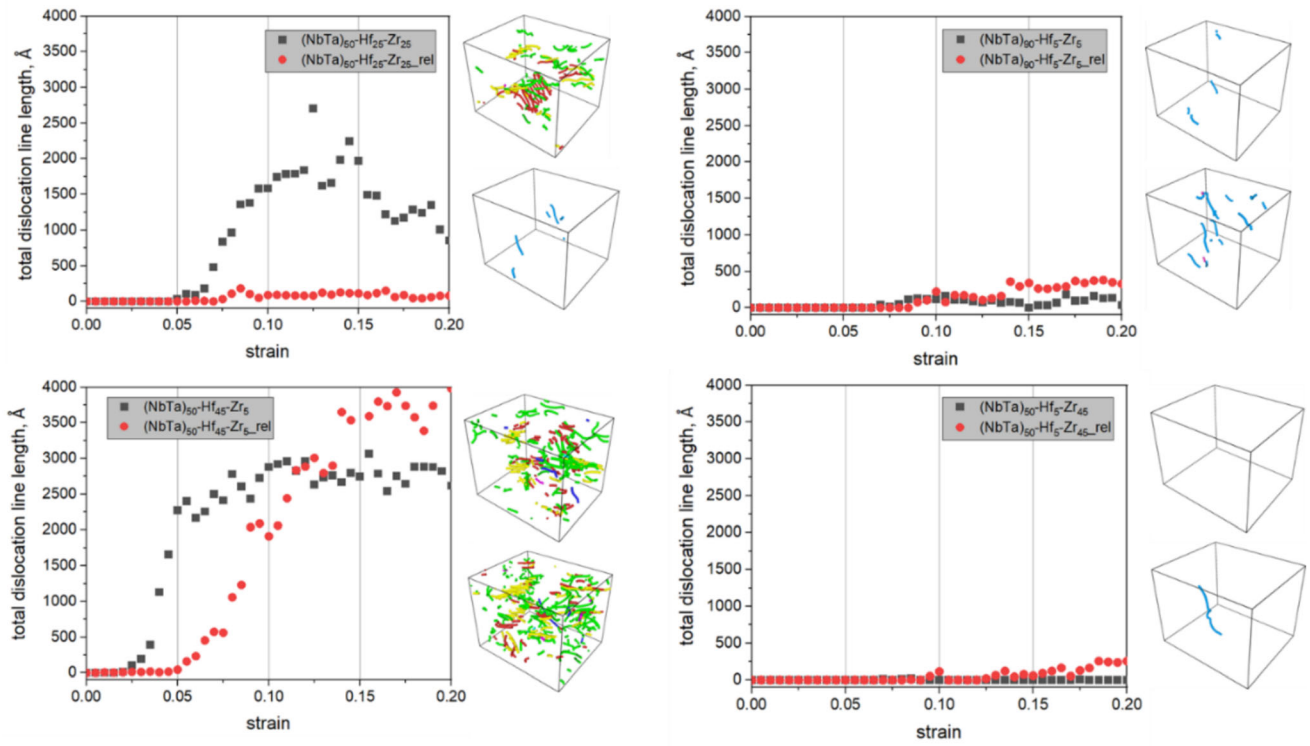

Fig. 13—Dependence of total dislocation line length on tensile strain. The corresponding dislocation structures at $\varepsilon_{xx} = 0.15$ for the alloys without relaxation (top) and with relaxation (bottom) are shown on the right side of each panel.

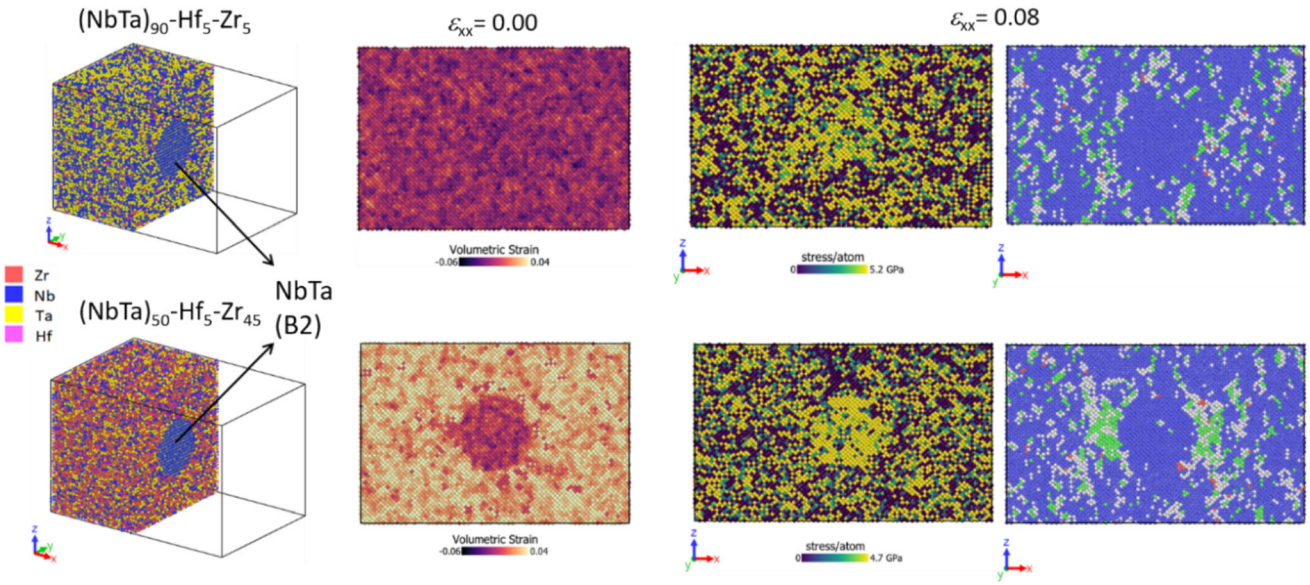

Fig. 14—MD models of single-crystalline $(NbTa)_{90}$–Hf_5–Zr_5 (on the top) and $(NbTa)_{50}$–Hf_{45}–Zr_5 (on the bottom) alloys with B2 NbTa spherical particle in the center. Only half of the samples are given here to see the particle inside. From left to right: volumetric strain per atom before deformation, stress distribution, and CNA in 20-Å-thick *xz* slices at $\varepsilon_{xx} = 0.08$.

accompanied by partial dislocation nucleation.[64] This can explain an increased strain hardening rate of the corresponding relaxed NC material after $\varepsilon_{xx} = 0.10$ compared to the non-relaxed $(NbTa)_{50}$–Hf_5–Zr_{45} (Figure 9). Apparently, due to small lattice parameter mismatch and the absence of Hf or Zr atoms, B2 particles of $(NbTa)_{90}$–Hf_5–Zr_5 can restrain dislocation generation at the interface and inside, leading to the reduced strain hardening rate in $(NbTa)_{90}$–Hf_5–Zr_5 (Figure 9).

Table II. Elastic Constants, Bulk Modulus *B*, Young's Modulus *E*, and Poisson's Ratio υ

	B, GPa	C_{11}, GPa	C_{12}, GPa	C_{44}, GPa	*E*, GPa	υ
$(NbTa)_{50}$–Hf_{25}–Zr_{25}	113.928	219.285	61.778	81.18	192.127	0.217
$(NbTa)_{90}$–Hf_5–Zr_5	165.179	308.977	94.207	83.485	264.952	0.230
$(NbTa)_{50}$–Hf_5–Zr_{45}	106.474	196.699	61.421	74.106	167.468	0.238
$(NbTa)_{50}$–Hf_{45}–Zr_5	120.757	221.561	70.548	84.392	187.484	0.242

Interatomic potentials for complex multi-component systems can overestimate or underestimate certain material characteristics, such as mixing enthalpy. Therefore, future work should compare these findings with results obtained using other available machine-learning-based potentials. Nevertheless, the present analysis provides meaningful insight into the influence of B2-type coherent clusters on the high-temperature deformation behavior of refractory HEAs.

It should be noted that the current study does not directly consider the interaction of dislocations with clusters and segregations. The Suzuki and Curtin models provide valuable frameworks for understanding dislocation–solute interactions and solution hardening in BCC alloys.[70–72] These approaches will be implemented in our future work to complement the present SRO-based analysis.

V. CONCLUSIONS

Combined MC/MD modeling is employed to investigate the effect of chemical composition on SRO in HEAs of the (NbTa)–Hf–Zr system. In addition, the effect of SRO on the tensile deformation behavior at 1000 K of four different NC HEAs of this system, namely $(NbTa)_{50}$–Hf_{25}–Zr_{25}, $(NbTa)_{50}$–Hf_5–Zr_{45}, $(NbTa)_{90}$–Hf_5–Zr_5, and $(NbTa)_{50}$–Hf_{45}–Zr_5, is studied in the work. It was revealed that by increasing the content of elements forming ordered clusters during the MC/MD relaxation process, which mimics diffusion, the chemical affinity between these elements can be reduced, thereby decreasing the tendency for clustering.

In general, elements of the atomic pairs Zr–Ta, Zr–Nb, Ta–Hf, and Nb–Hf do not form chemical bonds upon alloy relaxation and tend to be far from each other, while the atoms of the same type, namely Zr–Zr, Ta–Ta, Nb–Nb, and Hf–Hf, demonstrate the opposite behavior. As a result of relaxation, the chemical affinity between Zr and Hf and between Nb and Ta leads to the formation of the B2 clusters. The GB network affects the distribution of elements during the MC/MD relaxation of the NC alloys; the atoms of Zr, Nb, and Hf segregate at GBs, while Ta prefers to remain within the grains. This changes the composition of the alloys inside grains, which, as mentioned earlier, affects the SRO process.

SRO enhances the yield strength by 1.212, 0.765, 1.58, and 0.723 GPa of the NC HEAs $(NbTa)_{50}$–Hf_{25}–Zr_{25}, $(NbTa)_{90}$–Hf_5–Zr_5, $(NbTa)_{50}$–Hf_{45}–Zr_5, and $(NbTa)_{50}$–Hf_5–Zr_{45}, respectively. The strengthening effect is mainly attributed to the change in alloy composition inside grains and at GBs during the MC/MD relaxation. An increase of Ta content in grains and segregation of Zr and Hf atoms at GBs stabilize the BCC structure, which results in inhibiting phase transition and dislocation nucleation. Coherent B2 particles of NbTa can lead to additional strengthening of the HEAs through the load transfer mechanism when the particles endure higher stresses than the surrounding matrix, reducing internal stresses in it.

ACKNOWLEDGMENTS

The results of the project "FR-2025-75," carried out within the framework of the Basic Research Program at HSE University in 2025, are presented in this work.

DATA AVAILABILITY

No data are available for this study.

CONFLICT OF INTEREST

On behalf of all authors, the corresponding author states that there is no conflict of interest.

REFERENCES

1. E. Alabort, D. Barba, M.R. Shagiev, M.A. Murzinova, R.M. Galeyev, O.R. Valiakhmetov, A.F. Aletdinov, and R.C. Reed: *Acta Mater.*, 2019, vol. 178, pp. 275–87.
2. J.H. Martin, B.D. Yahata, J.M. Hundley, J.A. Mayer, T.A. Schaedler, and T.M. Pollock: *Nature*, 2017, vol. 549, pp. 365–69.
3. J.-W. Yeh, S.-K. Chen, S.-J. Lin, J.-Y. Gan, T.-S. Chin, T.-T. Shun, C.-H. Tsau, and S.-Y. Chang: *Adv. Eng. Mater.*, 2004, vol. 6, pp. 299–303.
4. B. Cantor, I.T.H. Chang, P. Knight, and A.J.B. Vincent: *Mater. Sci. Eng. A*, 2004, vol. 375, pp. 213–18.
5. Y.L. Chou, Y.C. Wang, J.W. Yeh, and H.C. Shih: *Corros. Sci.*, 2010, vol. 52, pp. 3481–91.
6. M.-H. Chuang, M.-H. Tsai, C.-W. Tsai, N.-H. Yang, S.-Y. Chang, J.-W. Yeh, S.-K. Chen, and S.-J. Lin: *J. Alloys Compd.*, 2013, vol. 551, pp. 12–18.
7. T. Nagase, S. Anada, P.D. Rack, J.H. Noh, H. Yasuda, H. Mori, and T. Egami: *Intermetallics*, 2013, vol. 38, pp. 70–79.
8. M.-H. Chuang, M.-H. Tsai, W.-R. Wang, S.-J. Lin, and J.-W. Yeh: *Acta Mater.*, 2011, vol. 59, pp. 6308–17.
9. O.N. Senkov, G.B. Wilks, D.B. Miracle, C.P. Chuang, and P.K. Liaw: *Intermetallics*, 2010, vol. 18, pp. 1758–65.
10. O.N. Senkov, D.B. Miracle, K.J. Chaput, and J.-P. Couzinie: *J. Mater. Res.*, 2018, vol. 33, pp. 3092–128.

11. O.N. Senkov, G.B. Wilks, J.M. Scott, and D.B. Miracle: *Intermetallics*, 2011, vol. 19, pp. 698–706.
12. Y. Zhang, B. Liu, R. Zhang, H. Liu, Y. Cao, J. Li, Q. Fang, and Y. Liu: *J. Mater. Res. Technol.*, 2023, vol. 23, pp. 1386–96.
13. Y. Xiao, X. Chang, X. Peng, and T. Fu: *J. Mater. Res. Technol.*, 2022, vol. 18, pp. 4169–80.
14. S. Wang, M. Wu, D. Shu, G. Zhu, D. Wang, and B. Sun: *Acta Mater.*, 2020, vol. 201, pp. 517–27.
15. Y. Zhang, Z. Bu, T. Yao, L. Yang, W. Li, and J. Li: *J. Alloys Compd.*, 2023, vol. 936, p. 168290.
16. Y. Jia, L. Zhang, P. Li, X. Ma, L. Xu, S. Wu, Y. Jia, and G. Wang: *Front. Mater.*, 2020, vol. 7, p. 172.
17. K.-K. Wong, H.-C. Hsu, S.-C. Wu, and W.-F. Ho: *J. Alloys Compd.*, 2021, vol. 868, p. 159137.
18. M. Hu, L. Wang, G. Li, Q. Huang, Y. Liu, J. He, H. Wu, and M. Song: *Intermetallics*, 2022, vol. 145, p. 107568.
19. M. Sahlberg, D. Karlsson, C. Zlotea, and U. Jansson: *Sci. Rep.*, 2016, vol. 6, p. 36770.
20. M.M. Nygård, G. Ek, D. Karlsson, M.H. Sørby, M. Sahlberg, and B.C. Hauback: *Acta Mater.*, 2019, vol. 175, pp. 121–29.
21. E.P. George, W.A. Curtin, and C.C. Tasan: *Acta Mater.*, 2020, vol. 188, pp. 435–74.
22. D.B. Miracle and O.N. Senkov: *Acta Mater.*, 2017, vol. 122, pp. 448–511.
23. Q. Ding, Y. Zhang, X. Chen, X. Fu, D. Chen, S. Chen, L. Gu, F. Wei, H. Bei, and Y. Gao: *Nature*, 2019, vol. 574, pp. 223–27.
24. X. Chen, Q. Wang, Z. Cheng, M. Zhu, H. Zhou, P. Jiang, L. Zhou, Q. Xue, F. Yuan, and J. Zhu: *Nature*, 2021, vol. 592, pp. 712–16.
25. R. Zhang, S. Zhao, J. Ding, Y. Chong, T. Jia, C. Ophus, M. Asta, R.O. Ritchie, and A.M. Minor: *Nature*, 2020, vol. 581, pp. 283–87.
26. S. Chen, Z.H. Aitken, S. Pattamatta, Z. Wu, Z.G. Yu, R. Banerjee, D.J. Srolovitz, P.K. Liaw, and Y.-W. Zhang: *Acta Mater.*, 2021, vol. 206, p. 116638.
27. Z. Sun, C. Shi, C. Liu, H. Shi, and J. Zhou: *Mater. Des.*, 2022, vol. 223, p. 111214.
28. S. Chen, Z.H. Aitken, S. Pattamatta, Z. Wu, Z.G. Yu, D.J. Srolovitz, P.K. Liaw, and Y.-W. Zhang: *Mater. Today*, 2023, vol. 65, pp. 14–25.
29. R. Wang, D. Duan, Y. Tang, Z. Lei, S. Li, R. Chen, C. Ma, Y. Wu, S. Bai, and Z. Lu: *Commun. Mater.*, 2023, vol. 4, p. 25.
30. X. Li: *Phys. Rev. Mater.*, 2023, vol. 7, p. 113604.
31. E. Ma: *Scripta Mater.*, 2020, vol. 181, pp. 127–33.
32. S. Chen, Z.H. Aitken, S. Pattamatta, Z. Wu, Z.G. Yu, D.J. Srolovitz, P.K. Liaw, and Y.-W. Zhang: *Nat. Commun.*, 2021, vol. 12, p. 4953.
33. W.-R. Jian, Z. Xie, S. Xu, Y. Su, X. Yao, and I.J. Beyerlein: *Acta Mater.*, 2020, vol. 199, pp. 352–69.
34. W. Ji and M.S. Wu: *Intermetallics*, 2022, vol. 150, p. 107707.
35. X. Huang, L. Liu, X. Duan, W. Liao, J. Huang, H. Sun, and C. Yu: *Mater. Des.*, 2021, vol. 202, p. 109560.
36. M. Beyramali Kivy and M. Asle Zaeem: *Scripta Mater.*, 2017, vol. 139, pp. 83–86.
37. H. Van Swygenhoven, P.M. Derlet, and A.G. Frøseth: *Nat. Mater.*, 2004, vol. 3, pp. 399–403.
38. L. Xie, P. Brault, A.-L. Thomann, X. Yang, Y. Zhang, and G.Y. Shang: *Intermetallics*, 2016, vol. 68, pp. 78–86.
39. W.-M. Choi, Y.H. Jo, S.S. Sohn, S. Lee, and B.-J. Lee: *npj Comput. Mater.*, 2018, vol. 4, p. 1.
40. J. Li, Q.H. Fang, B. Liu, Y.W. Liu, and Y. Liu: *RSC Adv.*, 2016, vol. 6, pp. 76409–19.
41. V.H. Ho, D.T. Ho, and S.Y. Kim: *Multiscale Sci. Eng.*, 2020, vol. 2, pp. 1–6.
42. X. Ou: *Mater. Sci. Technol.*, 2017, vol. 33, pp. 822–35.
43. Y.Z. Liu, J. Sun, H.L. Li, Y.Y. Song, S.P. Hu, X.G. Song, N. Guo, and W.M. Long: *J. Mater. Res.*, 2023, vol. 38, pp. 2838–51.
44. Y. Ikeda, K. Gubaev, J. Neugebauer, B. Grabowski, and F. Körmann: *npj Comput. Mater.*, 2021, vol. 7, p. 34.
45. Y. Chen, S.-W. Reng, J. Peng, and X.-B. Liu: *J. Mater. Res. Technol.*, 2023, vol. 24, pp. 3588–98.
46. X. Liu, D. Hua, W. Wang, Q. Zhou, S. Li, J. Shi, Y. He, and H. Wang: *J. Alloys Compd.*, 2022, vol. 920, p. 166058.
47. A. Tamm, A. Aabloo, M. Klintenberg, M. Stocks, and A. Caro: *Acta Mater.*, 2015, vol. 99, pp. 307–12.
48. T. Kostiuchenko, A.V. Ruban, J. Neugebauer, A. Shapeev, and F. Körmann: *Phy. Rev. Mater.*, 2020, vol. 4, p. 113802.
49. J. Li, H. Chen, H. Feng, Q. Fang, Y. Liu, F. Liu, H. Wu, and P.K. Liaw: *J. Mater. Sci. Technol.*, 2020, vol. 54, pp. 14–19.
50. D.-Q. Doan, T.-H. Fang, and T.-H. Chen: *Intermetallics*, 2021, vol. 131, p. 107079.
51. S. Yin, Y. Zuo, A. Abu-Odeh, H. Zheng, X.-G. Li, J. Ding, S.P. Ong, M. Asta, and R.O. Ritchie: *Nat. Commun.*, 2021, vol. 12, p. 4873.
52. W. Ji and M.S. Wu: *Scripta Mater.*, 2022, vol. 221, p. 114950.
53. A. Jarlöv, W. Ji, Z. Zhu, Y. Tian, R. Babicheva, R. An, H.L. Seet, M.L.S. Nai, and K. Zhou: *J. Alloys Compd.*, 2022, vol. 905, p. 164137.
54. L.S. Mantha, B.E. MacDonald, X. Mu, A. Mazilkin, J. Ivanisenko, H. Hahn, E.J. Lavernia, S. Katnagallu, and C. Kübel: *Acta Mater.*, 2021, vol. 220, p. 117281.
55. X.-G. Li, C. Chen, H. Zheng, Y. Zuo, and S.P. Ong: *npj Comput. Mater.*, 2020, vol. 6, p. 70.
56. N. Tuchinda and C.A. Schuh: *Acta Mater.*, 2022, vol. 226, p. 117614.
57. A.R. Kalidindi and C.A. Schuh: *Acta Mater.*, 2017, vol. 132, pp. 128–37.
58. P. Hirel: *Comput. Phys. Commun.*, 2015, vol. 197, pp. 212–19.
59. N. Metropolis, A.W. Rosenbluth, M.N. Rosenbluth, A.H. Teller, and E. Teller: *J. Chem. Phys.*, 1953, vol. 21, pp. 1087–92.
60. J. Mi Cowley: *J. Appl. Phys.*, 1950, vol. 21, pp. 24–30.
61. S. Plimpton: *J. Comput. Phys.*, 1995, vol. 117, pp. 1–19.
62. A. Stukowski: *Modell. Simul. Mater. Sci. Eng.*, 2009, vol. 18, p. 015012.
63. A. Jarlöv, W. Ji, R. Babicheva, Y. Tian, Z. Hu, H.L. Seet, L. Tan, F. Liu, Y. Liu, and M.L.S. Nai: *Mater. Des.*, 2024, vol. 240, p. 112840.
64. R.I. Babicheva, A.S. Semenov, A.A. Izosimov, and E.A. Korznikova: *Modelling*, 2024, vol. 5, pp. 1853–64.
65. P.P.P.O. Borges, R.O. Ritchie, and M. Asta: *Acta Mater.*, 2024, vol. 262, p. 119415.
66. Z.H. Aitken and Y.-W. Zhang: *MRS Commun.*, 2019, vol. 9, pp. 406–12.
67. R. Babicheva, A. Jarlöv, H. Zheng, S. Dmitriev, E. Korznikova, M.L.S. Nai, U. Ramamurty, and K. Zhou: *Comput. Mater. Sci.*, 2022, vol. 215, p. 111762.
68. V. Soni, O.N. Senkov, B. Gwalani, D.B. Miracle, and R. Banerjee: *Sci. Rep.*, 2018, vol. 8, p. 8816.
69. C. Han, R. Babicheva, J.D.Q. Chua, U. Ramamurty, S.B. Tor, C.-N. Sun, and K. Zhou: *Addit. Manuf.*, 2020, vol. 36, p. 101466.
70. S.I. Rao, C. Varvenne, C. Woodward, T.A. Parthasarathy, D. Miracle, O.N. Senkov, and W.A. Curtin: *Acta Mater.*, 2017, vol. 125, pp. 311–20.
71. S.I. Rao, B. Akdim, E. Antillon, C. Woodward, T.A. Parthasarathy, and O.N. Senkov: *Acta Mater.*, 2019, vol. 168, pp. 222–36.
72. C. Lee, F. Maresca, R. Feng, Y. Chou, T. Ungar, M. Widom, K. An, J.D. Poplawsky, Y.-C. Chou, and P.K. Liaw: *Nat. Commun.*, 2021, vol. 12, p. 5474.